The μ opioid receptor crystal structure with BU72 is a covalent adduct

Thomas A. Munro

School of Life and Environmental Sciences, Deakin University, Melbourne, Australia

Current email: thomas@munro.com

Abstract

The first crystal structure of the active μ opioid receptor (μOR) exhibited several unexplained features. The ligand BU72 exhibited many extreme deviations from ideal geometry, along with unexplained electron density around the benzylic carbon. I previously showed that inverting the benzylic configuration resolved these problems, establishing revised stereochemistry of BU72 and its analog BU74. However, another problem remains unresolved: additional unexplained electron density contacts both BU72 and a histidine residue in the N-terminus.

Here I show that these short contacts and uninterrupted density are inconsistent with non-covalent interactions. Therefore, BU72 and μOR form a covalent adduct through an unmodeled atom, and the published model as two separate entities is incorrect. A subsequently proposed magnesium complex is also inconsistent with multiple lines of evidence. However, oxygen fits the unexplained density well. While the proposed structure is tentative, similar oxygen-bridged adducts have been reported previously in the presence of reactive oxygen species. Moreover, known sources of reactive oxygen species were present: HEPES buffer, nickel ions, and a sequence motif that forms redox-active nickel complexes. This motif contacts the unexplained density.

The adduct exhibits severe strain, and the tethered N-terminus forms contacts with adjacent residues. These forces, along with the nanobody used as a G-protein substitute, would be expected to influence the receptor conformation. Consistent with this, the intracellular end of the structure differs markedly from subsequent structures of active μOR bound to G_i protein. These later structures are likely to be more accurate templates for docking and molecular dynamics simulations. The possibility of reactions like this should be considered in the choice of protein truncation sites and purification conditions, and in the interpretation of excess or unexplained density.

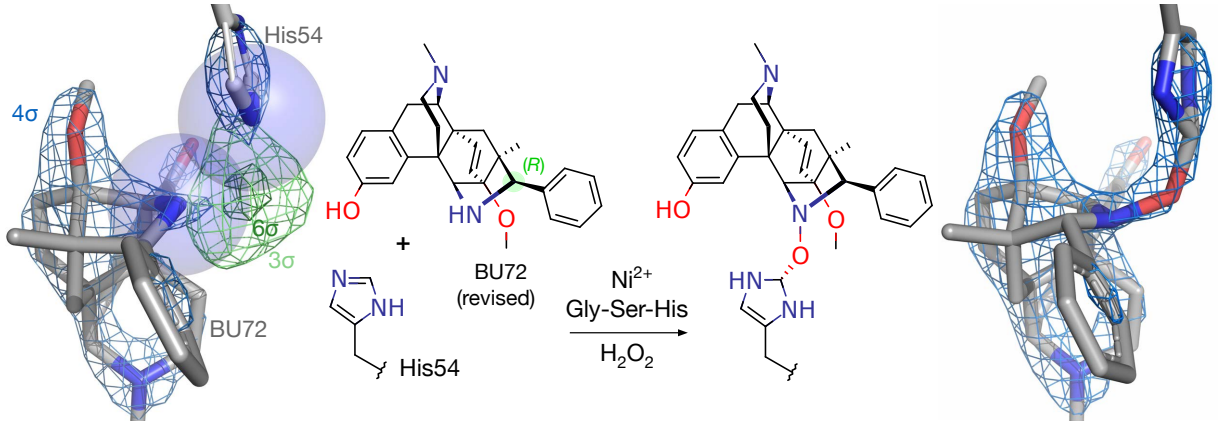

Graphical abstract

Keywords

BU72; covalent adduct; crystal structure; μ opioid receptor; revised stereochemistry

Introduction

BU72 is a μ opioid of exceptionally high affinity and potency (**Figure 1**) (1; 2). Its dissociation constant (K_i) for μOR ranges from 0.15 nM in crude brain membranes (1), to lower values in transfected cell membranes (2; 3), and as low as 0.01 nM for purified μOR with G_i protein (3). Very few ligands for any protein exceed this extraordinary affinity, which is considered an effective upper bound on the strength of non-covalent binding (4).

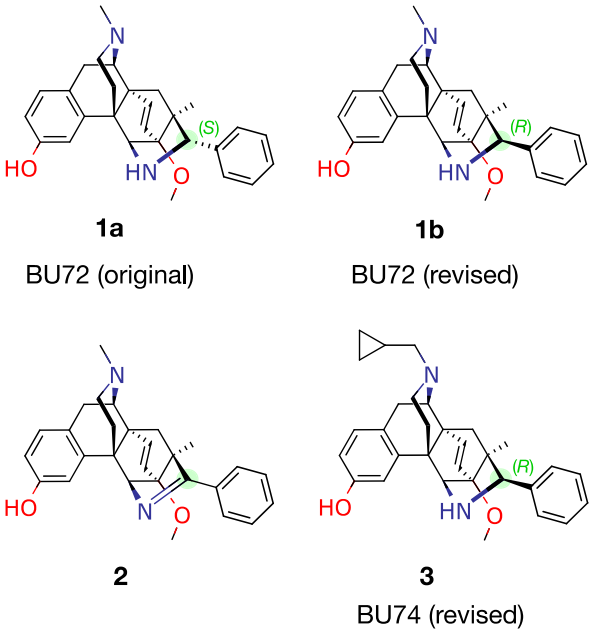

Figure 1: Structures of BU72 and analogs.

BU72 was the ligand in the first crystal structure of active μOR (3). As noted there, the electron density exhibited two unexplained features. Firstly, fitting the published structure of BU72 (**1a**, **Figure 1**) required a near-planar orientation of the phenyl group, an implausibly high-energy conformation that required many extreme deviations from ideal geometry and left unexplained density around the benzylic carbon (**Figure 2**a). The authors considered the possibility that the ligand was actually imine **2** (**Figure 1**), whose planar sp^2 benzylic carbon would resolve this problem, but this was not detected

in mass spectra of the crystallization mixture (3). In a preprint, I proposed an alternative: a revised structure for BU72 with the phenyl group in the opposite (*R*) configuration (**1b, Figure 1**) (5). Revised structure **1b** fits in a low-energy conformation, eliminating the geometric outliers and unexplained density around the phenyl group, and yielding superior validation metrics (**Figure 2**b) (5).

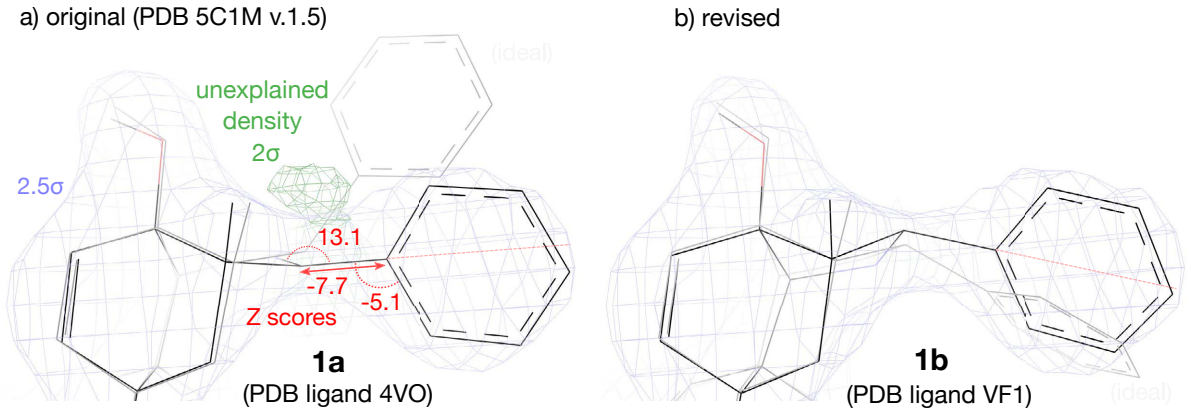

Figure 2: Phenyl group geometric outliers and unexplained electron density for original (**1a**) and revised (**1b**) structures of BU72. Colors: fitted structures (*black*); ideal structures (*grey)*; geometric outliers in the phenyl group (Z scores, *red*); 2*F*o-*F*c density (2.5σ, *violet*); *F*o-*F*c omit density (2σ, *green*). Adapted from (5).

The original proposed configuration of **1a** was based on unpublished nuclear Overhauser effect (nOe) data, and the basis for the necessary NMR assignments was not stated (1; 2). Thus, no published data support the original assignment, and the structure of BU72 should be revised to **1b**. The authors of the crystal structure, including the lead author of the original synthesis, accepted this revision in a correction notice (6). However, the revised structure was not shown. Protein Data Bank entry 5C1M was also corrected (version 2.0). Note that the structure of the analog BU74 (**3**, **Figure 1**) should also be revised, since they differ only in the N-substituent (7); their

synthetic routes diverge after establishment of the phenyl configuration, and the benzylic hydrogen is not exchangeable.

A second puzzling feature of the crystal structure remains unexplained after this revision. The truncated N-terminus of the receptor, which is highly disordered and hence unresolved in other opioid receptor structures, unexpectedly intrudes into the binding pocket (3). The third residue, His54, clashes with BU72. The overlapping atoms also contact a pocket of strong, unexplained electron density (**Figure 3**). The atom responsible for this density could not be identified; experiments testing for an alternative ligand structure or a coordinated heavy metal were unsuccessful (3). The atom was ultimately omitted from the model altogether. The revised model with **1b** (5C1M v.2) reduced the clash between ligand and receptor, but did not account for the unexplained density.

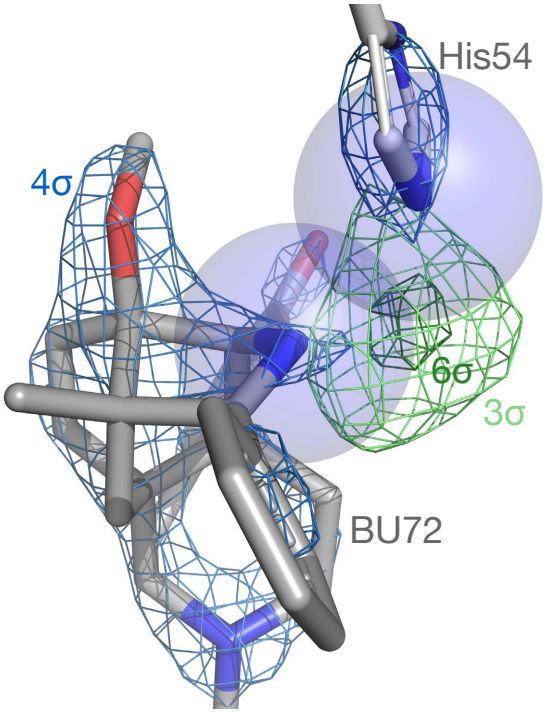

Figure 3: Clashes and unexplained density between BU72 and His54 in the original model (5C1M v.1.5). *2F*o-*F*c density (*blue*) and *F*o-*F*c omit density (*green*) are shown at the indicated levels. Clashing N atoms are shown as spheres.

Other authors later proposed that the missing atom is a magnesium ion (8). This fitted the unexplained density well, while lithium, sodium, nickel, and zinc ions did not (8). Bond lengths were not given, but were reportedly consistent with a magnesium coordination complex (9).

Results and Discussion

The missing atom is not magnesium

I first refined a complex with the previous candidate, Mg^{2+}. Consistent with the earlier reports (8; 9), this gave a good fit, with no excess or unexplained density above 2.5σ (**Figure 4**). However, contrary to the prior reports, the N–Mg bonds were unrealistically short (1.9 and 1.7 Å). Compare the N–Mg bond lengths in structures of subatomic

resolution: 2.19 ± 0.06 Å (10). These bonds are thus extreme outliers, with Z scores of -5 and -9, respectively. The high resolution of the structure (2.1 Å) allows strong conclusions about bond lengths, with a diffraction precision index (DPI) of 0.22 Å for the Mg^{2+} ion (11). Note also that the ion is not centered in the density even with these unrealistically short distances, suggesting that the actual bonds must be shorter still (**Figure 4**). This resulted in a poor real-space R value (RSR) of 0.32 for the Mg^{2+} ion, despite good values for His54 (0.11) and BU72 (0.08).

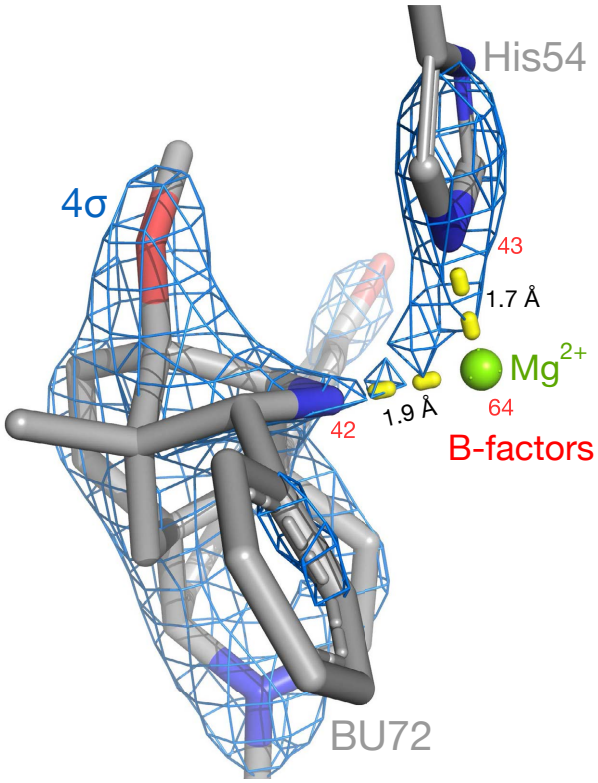

Figure 4: Proposed magnesium complex (8), with bond lengths and B-factors (*red*).

A later report from the same group added a third bond to the model (9), from Mg^{2+} to Tyr148^{3x33} (using GPCRdb numbering (12)) (**Figure 5**). However, this would require an O–Mg bond length of 3.1 Å; compared with high-resolution structures (2.10 ± 0.04 Å), this is untenable (Z = 25) (10). It is instead consistent with a hydrogen bond to another element. Note also the large gap in the electron density along this proposed bond, unlike the strong and uninterrupted density for the bonds to BU72 and His54

(**Figure 5**). Additionally, note the highly asymmetrical geometry required, with a bond angle of 105°, compared to 90° for the N atoms; magnesium complexes are symmetrical (10).

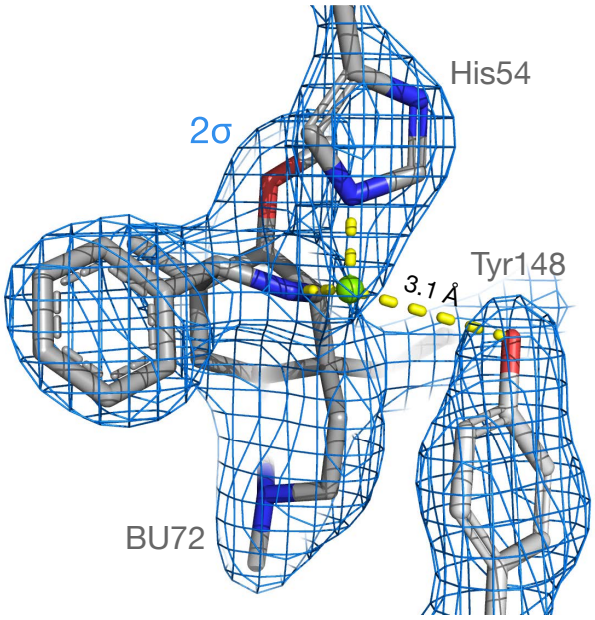

Figure 5: Proposed third bond from Mg^{2+} to $Tyr148^{3x33}$ (9).

Other evidence against Mg^{2+} was revealed by CheckMyMetal (13). Five of the eight parameters evaluated were classed as outliers, including three that strongly suggest a misidentified element:

- A much higher temperature factor (B-factor) than its bonding partners (**Figure 4**); since bonds transmit thermal motion, this is implausible (14).
- Bonding to an amine, which is positively charged at this pH (7.5), while Mg^{2+} favors neutral or negatively-charged bonding partners (13; 15).
- An incomplete coordination sphere. The expected number of bonds is six, or in rare cases four or five; a value of two is extremely rare in high-resolution structures (16).

While it could be speculated that unresolved water molecules complete the coordination sphere, this is implausible since the rest of the complex is resolved with

full occupancy, as are many structured water molecules elsewhere in the binding pocket (3).

Finally, no source of magnesium is mentioned in the experimental method (3). Collectively, the above lines of evidence firmly exclude Mg^{2+} as a candidate.

The missing atom forms covalent bonds to both BU72 and His54

While the element is evidently misidentified, the fit of the Mg^{2+} ion to the density does firmly establish a non-hydrogen atom in this approximate position. As noted above, this missing atom is likely nearer to both His54 and BU72 than the modelled position of Mg^{2+}; that is, < 1.9 Å from each (**Figure 4**). This is much too close for non-covalent interactions (≥ 2.4 Å) (17), which would also not result in strong, uninterrupted electron density connecting the three atoms. For instance, the protonated tertiary amine of BU72 forms a charge-assisted hydrogen bond (salt bridge) to aspartate $Asp147^{3x32}$ (**Figure 6**); these are among the shortest of all noncovalent interactions (17). Nonetheless, the N···O distance is 2.6 Å, and the regions of high electron density are widely separated, in striking contrast to the continuous density surrounding the purported Mg^{2+} complex (**Figure 6**). Therefore, the unidentified atom is covalently bonded to both BU72 and μOR; that is, they form an adduct.

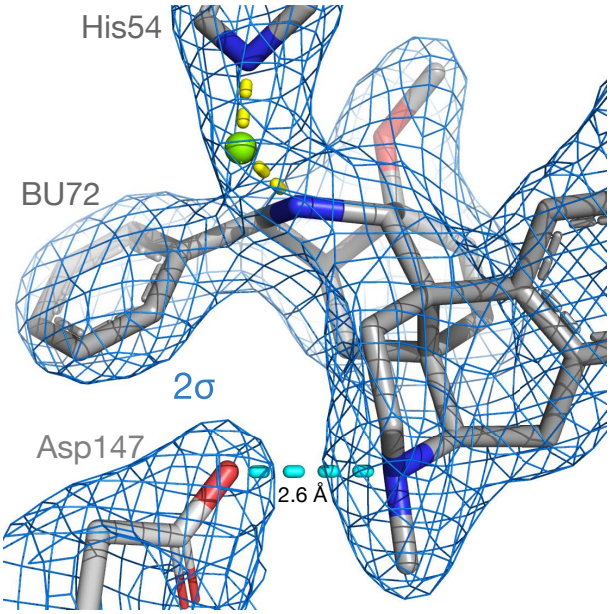

Figure 6: Electron density comparison of the proposed Mg^{2+} complex with the salt bridge to Asp147[3x32].

While this evidence does not establish the identity of the missing atom, it does establish that the published model is incorrect. A model of the adduct with an unidentified atom would be correct, albeit incomplete; hundreds of PDB structures contain unidentified atoms (ligand code UNX). However, the published model, in which BU72 and the receptor are discrete entities, is not consistent with the evidence.

The missing atom is very unlikely to be a metal, but may be oxygen

The CheckMyMetal validation report for magnesium suggested alternative metals as better candidates: copper, zinc, nickel, cobalt, and iron. However, each of these also gave multiple outliers when validated. Also, of these metals, only nickel was present during preparation of the crystals (in the affinity column). The bond lengths are more plausible than for magnesium, since N–Ni bonds are short (1.88 ± 0.03 Å) (10). However, as noted above, nickel did not fit the electron density, leaving a substantial excess (8); further evidence against nickel and other heavy metals is the lack of anomalous scattering noted in the original report (3).

The only metal in the buffer solution, sodium, also gave five CheckMyMetal outliers, including even more extreme outliers from typical N−Na bond lengths (2.46 ± 0.02 Å, Z = -29 and -40) (10), and a much worse fit to the density than magnesium (8). Indeed, no metal forms coordination bonds to N shorter than 1.76 Å (10). It is thus extremely implausible that the missing atom is a metal.

Given the above, it appears that the missing atom is a non-metal approximately isoelectronic with magnesium, but that forms shorter bonds. The element must also be at least divalent, and can probably form hydrogen bonds given its distance to Tyr148^{3x33} (~3.1 Å). One candidate meeting these criteria is oxygen; based on electron density alone, water molecules are frequently misidentified as magnesium (15; 18).

A known source of reactive oxygen species contacts the unexplained density

Formation of an oxygen-bridged adduct between the secondary amine of BU72 and the imidazole ring of His54 would require harsh conditions. Reactive oxygen species (ROS), for instance, can oxidize secondary amines (19) and histidine (20). But how might these arise? Surprisingly, several potential sources of ROS were present. The BU72-μOR complex was purified and crystallized in HEPES buffer, which generates hydrogen peroxide on exposure to light (21). HEPES has also been reported to enhance metal-catalyzed generation of other ROS from hydrogen peroxide (22). A further potential source is the N-terminus, which contains a sequence motif known to generate ROS. The N-terminus used was truncated, leaving glycine as the first residue and histidine as the third (3). This sequence motif (Gly-Xaa-His) forms redox-active nickel coordination complexes (23). Moreover, nickel was present, in the affinity column used for purification (3); the Gly-Xaa-His motif can capture Ni^{2+} ions from these columns (24; 25; 26). The resulting square planar nickel complexes catalyze the

decomposition of hydrogen peroxide to other ROS such as hydroxyl radicals (23). Thus, the conditions used were sufficient to generate ROS immediately adjacent to His54, potentially oxidizing both the residue itself and BU72.

A search of PDBeMotif (27) revealed eight protein structures in which square planar Gly-Xaa-His-Ni^{2+} complexes were resolved: PDB entries 1JVN, 1XMK, 2RJ2, 3RDH, 3UM9, 3ZUC, 4I71, and 4OMO. In three cases, the nickel was not added during crystallization, but unexpectedly captured during affinity chromatography: 1JVN (24), 3UM9 (25), and 3ZUC (26). Intriguingly, in 1JVN the electron density was not consistent with the expected ligand structure; no density supported several of the atoms, suggesting partial decomposition (24). The buffer used, PIPES, is an analog of HEPES that also generates hydrogen peroxide (28) and other ROS (22). This provides a plausible explanation for the decomposition of the ligand.

Proposed structure of an oxygen-bridged adduct

Two previous reports of adduct formation between aminoxyl radicals and imidazole rings are shown in **Scheme 1a** (20; 29). These suggested potential structure **6** for an adduct between BU72 and His54 (**Scheme 1b**). The stereochemistry of the bond to the modified histidine residue was dictated by the observed density. A possible intermediate aminoxyl radical is also shown; these can form from oxidation of secondary amines by ROS (19).

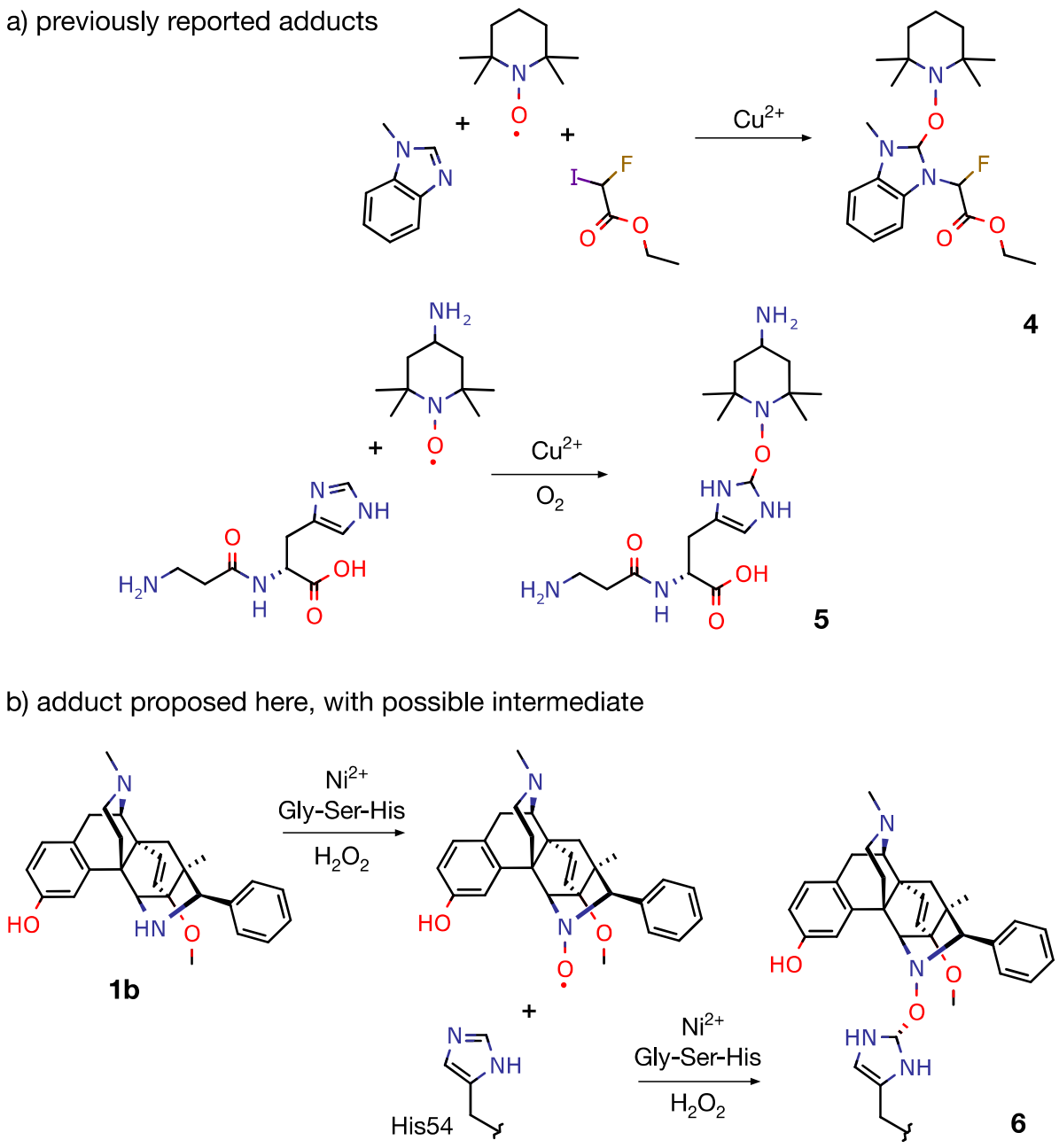

Scheme 1: a) Reported adducts **4** ((29), Scheme 2) and **5** ((20), Figure 7c). **b)** Adduct **6** proposed here, with a possible aminoxyl intermediate.

Oxygen-bridged adduct 6 fits the unexplained density

Modeling and refinement of adduct **6** gave an excellent fit, with no excess or unexplained density even at 2σ (**Figure 7**). Both bonds to oxygen were of typical length (1.5 Å), and were resolved up to 4.2σ – that is, higher density than most of the ligand itself and surrounding side-chains. Unlike Mg^{2+}, the oxygen atom was well centered in

the density. Oxygen also gave a superior B-factor to Mg^{2+}, both lower and consistent with its bonding partners, making this a much more plausible candidate element (**Figure 7**) (14). The lower B-factor for oxygen results in a more precise fit (DPI 0.14 vs 0.22 Å). Indeed, it is among the most precisely-resolved atoms in the entire structure, which is itself the highest-resolution structure of μOR to date. The bridging oxygen and modified histidine moiety make favorable polar contacts with Tyr148^{3x33}, which are close to the length of a weak hydrogen bond.

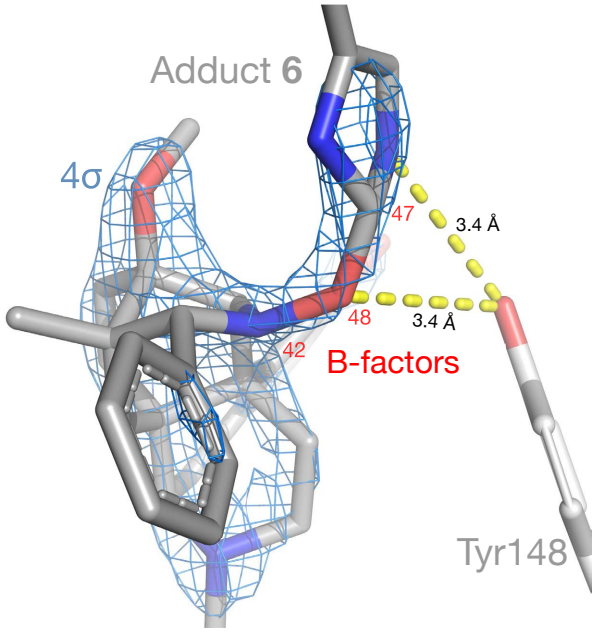

Figure 7: Fit of adduct **6** to density, with B-factors (*red*) and polar contact distances to Tyr148^{3x33}.

The adduct is highly strained

The geometry of the adduct gave acceptable validation metrics, which were superior to the original model (**Table 1**).

Table 1: Geometry relative to GRADE restraints, and fit to electron density from PDB validation.

Structure	5C1M v1.5	Adduct
Geometric outliers (|Z| > 2)	26	10
Severe outliers (|Z| > 5)	9	1
Bond angle root mean square Z (RMSZ)	3.23	1.52
Bond length root mean square Z (RMSZ)	3.32	1.13
Real-space correlation coefficient (RSCC)[a]	0.914	0.951
Real-space R (RSR)	0.090	0.081

[a] Lower values are better except for RSCC

The only severe outlier was the bond angle at the bridging oxygen (131° vs the ideal, 109°: Z = 7.2). There are several indications that this is real strain rather than a fitting artefact, however. The angle is clearly resolved at high density, and is consistent with tension from the tethered N-terminus. The phenyl group is bent 11° out of plane, consistent with being pulled against the adjacent residue Ile144 by the same tension (**Figure 8**). This bend is also clearly resolved, and is comparable to those seen in severely strained aromatic residues at subatomic resolution (30). It also yields a more complementary fit to Ile144 than the original model, as well as eliminating another small pocket of unexplained density (**Figure 8**).

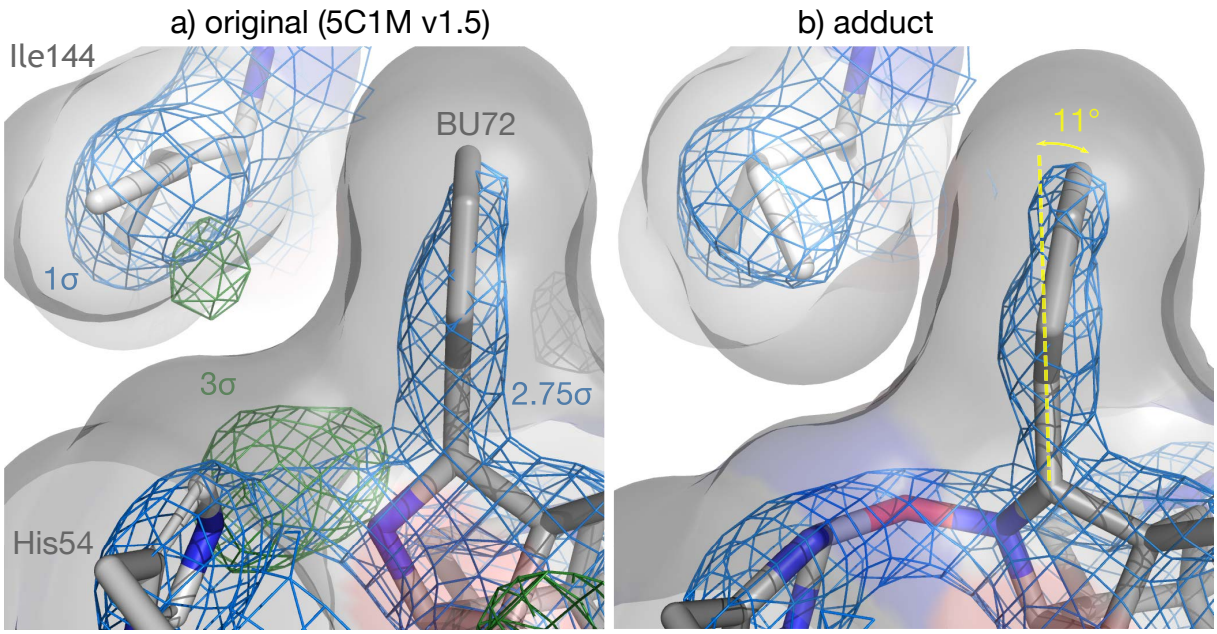

Figure 8: Fit of phenyl group to adjacent residue Ile144, shown with solvent-accessible surfaces (**a:** original model (5C1M v.1.5); **b:** adduct).

Strain is also evident in the N-terminus itself: in both this model and the original (5C1M v.1.5), Thr60 adopts a rare and high-energy *cis*-peptide bond, and there are many energetically unfavorable clashes along the peptide backbone (**Figure 9**).

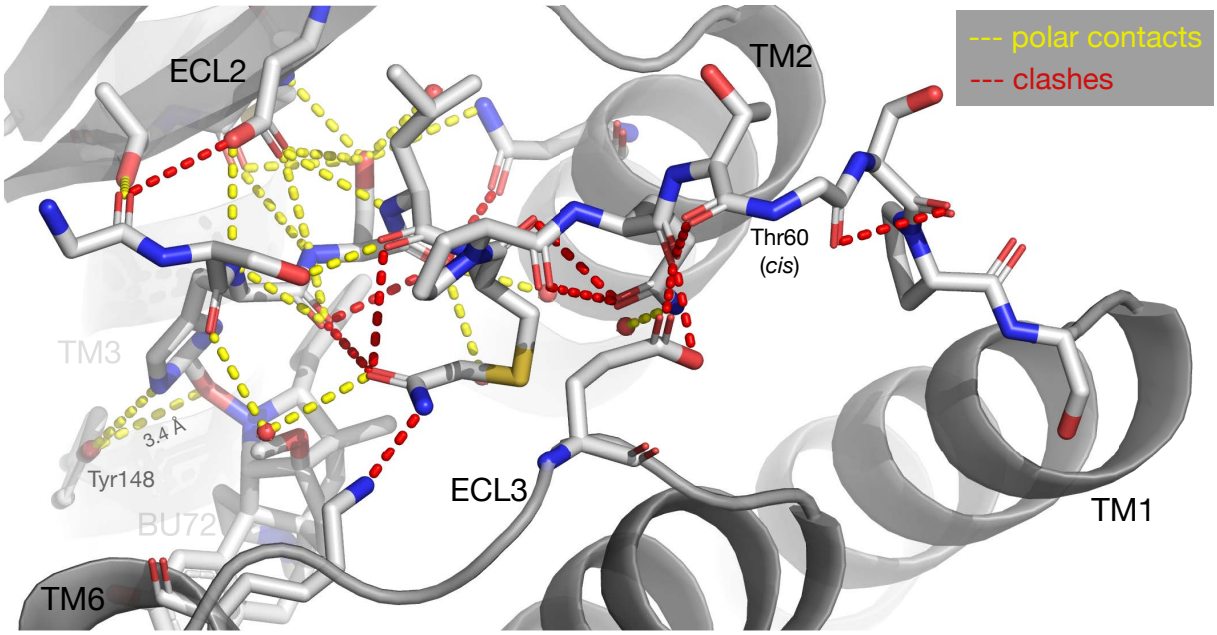

Figure 9: Polar contacts (<3.6 Å) and clashes of the tethered N-terminus in the adduct model. Note the high-energy *cis*-peptide bond at Thr60.

Alternate modelling can eliminate the *cis*-peptide bond, as in the revised version of the original model (5C1M v.2). However, this results in a worse fit to the density, which is extremely weak in this region: several side-chains and even parts of the backbone are unresolved at 1σ, yielding eight RSR outliers in the N-terminus, five of which are severe (**Figure 10**). Atomic displacements in the N-terminus are also extremely high: the occupancy-weighted average B-factor (OWAB) of the last seven residues (58-64) are higher than 95% of residues in the structure. Indeed, Gln59 has the highest value in the entire structure, 159 $Å^2$, compared to a median of 46. The above features (poor density coverage, high B-factors, clashes and a probable *cis*-peptide bond) imply that the N-terminus is constrained in an extremely unfavorable high-energy state by the tethered ligand.

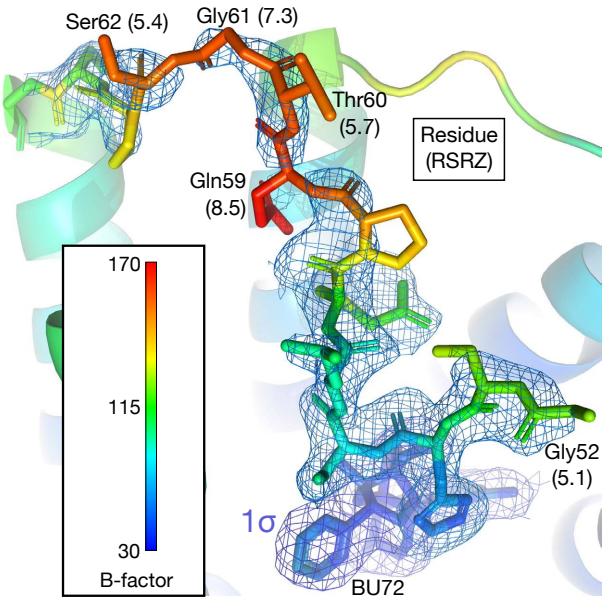

Figure 10: The N-terminus in the revised version of the original model (5C1M v.2), colored by B-factor. Note poor electron density coverage for some residues; RSRZ scores > 5 (severe outliers) are given in brackets.

Despite the very strong interactions apparent between BU72 and His54, removal of the side chain of His54 by receptor mutagenesis had no detectable effect on the affinity or potency of BU72 (3). This seeming paradox, however, is consistent with the mechanism proposed here. Since the full-length receptor was used for the assays, lacking the Gly-Xaa-His motif required for nickel complexation, adduct formation could not occur. Thus, binding would be unaffected by the presence or absence of His54.

Adduct strain, N-terminal contacts, and nanobody Nb39 distort the receptor, confounding inferences about the active conformation

The forces required to tether the ligand and N-terminus in high-energy conformations must affect the rest of the receptor. Compounding this, the N-terminus makes numerous strong contacts throughout the binding pocket, including a dense network of polar contacts and clashes with transmembrane helices and extracellular loops (**Figure 9**).

In addition to the strain in the N-terminus and the contacts it makes, another factor likely to influence the receptor conformation is the intracellular binding partner used, G-protein mimetic nanobody Nb39. Nanobodies are known to yield slightly different receptor conformations than G-proteins (31).

Indeed, four subsequent structures of active μOR bound to G_i protein (32; 33; 34) differ markedly from the BU72-μOR-Nb39 structure at the intracellular end. In all these active structures, the intracellular end of TM6 shifts outwards relative to the inactive state, a well-known step in GPCR activation (35). However, the shift for BU72-μOR-Nb39 is in a different direction than in the G_i-bound structures, leaving TM5 much closer to TM6, and forcing intracellular loop 3 outwards (**Figure 11**). This difference appears to be largely due to Nb39, since the structure of κOR bound to the same nanobody is very similar (**Figure 11**) (36).

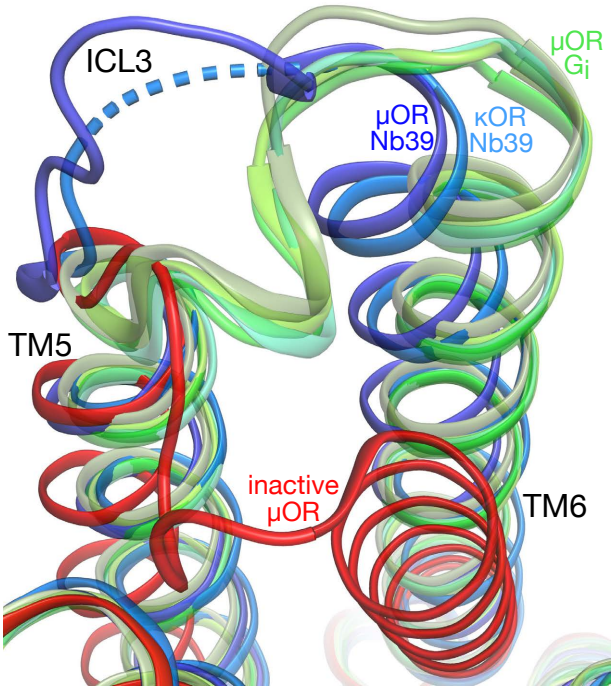

Figure 11: Overlay of TM5, TM6 and ICL3 when inactive, or bound to Nb39 or G_i protein. PDB codes: 5C1M (BU72-μOR-Nb39); 6B73 (κOR-Nb39); 6DDE, 7SBF, 7SCG, and 7U2L (μOR-G_i); 7UL4 (inactive).

As expected from the greater distance between TM5 and TM6, several conserved residue shifts that occur during activation (31) differ markedly in the subsequent μOR-G_i structures (**Figure 12**). These include Tyr336^{7x53}, part of the important NPxxY motif (31). Whether due to the influence of the adduct, the nanobody or both, these differences from the μOR-G_i structures are likely to be artefacts, and the latter provide preferable templates for modeling the G_i-bound active conformation.

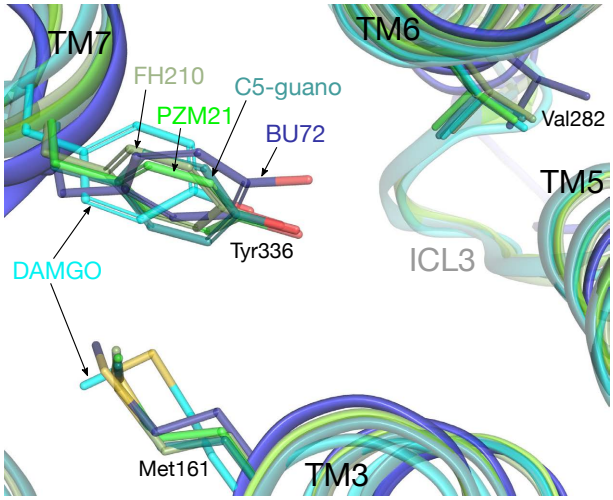

Figure 12: Differences from G_i-bound structures in three μOR residues that shift during activation: Met161^{3x46}, Val282^{6x37}, and Tyr336^{7x53}. Structures are labeled by ligand: BU72 (PDB: 5C1M), DAMGO (6DDE), PZM21 (7SBF), FH210 (7SCG), and C5-guano (7U2L).

Proposed experimental tests of adduct formation

In the original study, a search for alternative ligands to account for the unexplained density was unsuccessful. The mass spectrum of the crystallization mixture revealed a molecular ion consistent with BU72, but no others of similar mass (3). However, the intact adduct would not be detectable in solution, and one decomposition product per binding site would yield negligible concentrations relative to saturating BU72. An alternative test would be for modification of His54: proteolysis of the receptor and mass

spectrometry of the fragments should reveal either the adduct or decomposition products. A simpler alternative would be to substitute a short Gly-Xaa-His-containing peptide for the receptor, although this might also result in side-reactions. The initial nickel complex itself should be detectable spectroscopically, and may indeed give a noticeable yellow color to the solution (23).

An obstacle to isolation of the adduct may be instability. Previously-reported adducts **4** and **5** were not isolated, but detected only by mass spectrometry as reaction intermediates (20; 29). However, the tethered conformation of the N-terminus separates Gly52 from His54, rendering a nickel complex between the two residues impossible (**Figure 10**). Thus, adduct formation would liberate the ion and end the catalytic cycle. Moreover, the 'lid' formed by the N-terminus almost entirely occludes the binding pocket (3), leaving only a narrow tunnel filled with structured water molecules. Thus, the adduct bonds are sterically shielded, which may inhibit further reactions.

Wider implications, and precautions against ROS generation

The risk of unexpected complexes and oxidations like this is not specific to the structures discussed here. The conditions that led to these reactions, in both this case and previously (24), are widely used. Many common methods for the cleavage of fusion proteins (thrombin, factor Xa, tobacco etch virus protease, and rhinovirus 3C protease) leave glycine as the N-terminal residue (37). Unsurprisingly then, the N-terminal Gly-Xaa-His motif is common in the Protein Data Bank, appearing in >7,000 sequences (~4% of the total). Nickel affinity columns are also widely used. Many of these proteins would therefore be expected to form Gly-Xaa-His-Ni^{2+} complexes. However, the first few residues of the N-terminus are almost invariably disordered: 97% of human proteins have disordered terminal residues (38), and 42% of all disordered residues

are in the N-terminus (39). Thus, these complexes are very unlikely to be resolved, and are therefore likely to go undetected. Peroxide-generating buffers such as HEPES are also ubiquitous; thus, quite common procedures for protein preparation inadvertently generate ROS. Oxidation by ROS can have many undesirable effects on proteins, from modifying side chains (which may influence the overall conformation) to cleaving the amide backbone (40).

The possibility of reactions like this should be considered in the choice of truncation sites and purification conditions for protein isolation. Generation of nickel complexes, ROS, and subsequent reactions could be prevented by choosing a different cleavage site (with a third residue other than histidine) or a nickel-free purification method. Where a nickel complex is desired, for instance to promote crystallization (24) or assist in phasing (26), a non-piperazine buffer such as Tris or MES could be used to avoid or reduce ROS generation (41).

Conclusion

In summary, the density observed between BU72 and His54 is not consistent with non-covalent interactions or a metal coordination complex, and must instead represent covalent bonds to a non-metal atom, approximately isoelectronic with Mg^{2+}. The density firmly establishes the presence of this atom and two covalent bonds, and suggests a polar contact with Tyr148. While this evidence does not unambiguously identify the atom, it does establish that the published model is incorrect. The use of conditions known to generate ROS, along with adducts reportedly previously in the presence of ROS, suggest a tentative structure and mechanism for the formation of an oxygen-bridged adduct. All features examined are consistent with this proposal.

The structure differs in several respects from subsequent structures of μOR bound to G_i protein, likely due to the use of a nanobody, severe strain within the N-terminus, and

its contacts with surrounding residues. These subsequent μOR-G_i structures are likely to be more accurate templates of the active receptor for docking and simulations of molecular dynamics. Oxidative artefacts like this can be prevented by careful choice of truncation sites and purification conditions.

Experimental

Starting from the previously reported model (5) of μOR with **1b**, Mg^{2+} was added to the center of the unexplained density with sphere refinement using Coot (42) in CCP4i2 (43), and uploaded with the original structure factors to PDB-REDO server (44) for automated refinement. The resulting complex was submitted to CheckMyMetal (15) for validation; all suggested alternative metals were also resubmitted for validation.

The ideal structure and geometric restraints of the **1b**-histidine adduct were generated using GRADE server (45). BU72 was deleted from the original model, His54 was mutated to the adduct, and the model fitted and refined as above. Because the PDB validation report did not evaluate the adduct's geometry, ligand distortions were tabulated in Coot (comparing ideal values and standard deviations from GRADE with modeled values), and used to calculate Z scores (Supporting Information File 11). The residues shown in **Figure 12** were selected from a previously published comparison of active structures, showing differences between PDB 5C1M and 6DDE (see Figure 2-Source data 1 in (31)). Diffraction precision index was calculated using Online_DPI (11). Figures were created using Inkscape, Marvinsketch, and Pymol (46).

Supporting Information

Coordinates and structure factors for the adduct have been deposited in the PDB (entry 8E0G). An interactive comparison of the adduct and original model is available at: molstack.bioreproducibility.org/p/Y7FU

Supporting Information File 1:

File Name: BU72-Mg-muOR model.cif

File Format: mmCif

Title: Coordinates of the BU72-Mg^{2+}-μOR complex

Supporting Information File 2:

File Name: BU72-Mg-muOR phases.mtz

File Format: MTZ

Title: Structure factors of the BU72-Mg^{2+}-μOR complex

Supporting Information File 3:

File Name: BU72-Mg-muOR validation report.pdf

File Format: PDF

Title: PDB validation report for the BU72-Mg^{2+}-μOR complex (PDF)

Supporting Information File 4:

File Name: BU72-Mg-muOR validation report.xml

File Format: xml

Title: PDB validation report for the BU72-Mg^{2+}-μOR complex (xml)

Supporting Information File 5:

File Name: BU72-muOR adduct model.cif

File Format: mmCif

Title: Coordinates of the BU72-μOR adduct

Supporting Information File 6:

File Name: BU72-muOR adduct phases.mtz

File Format: MTZ

Title: Structure factors of the BU72-μOR adduct

Supporting Information File 7:

File Name: BU72-muOR adduct validation report.pdf

File Format: PDF

Title: PDB validation report for the BU72-μOR adduct (PDF)

Supporting Information File 8:

File Name: BU72-muOR adduct validation report.xml

File Format: xml

Title: PDB validation report for the BU72-μOR adduct (xml)

Supporting Information File 9:

File Name: BU72-histidine adduct ideal structure.pdb

File Format: pdb

Title: Ideal coordinates of BU72-histidine adduct **6** (GRADE server)

Supporting Information File 10:

File Name: BU72-histidine adduct restraints.cif

File Format: mmCif

Title: Geometric restraints of BU72-histidine adduct **6** (GRADE server)

Supporting Information File 11:

File Name: GRADE ligand outliers.xlsx

File Format: xlsx

Title: Geometric outliers of BU72 and the BU72-μOR adduct (GRADE server)

Supporting Information File 12:

File Name: chemical structures.cml

File Format: cml

Title: Chemical structures (structural formulae) of the small molecules

Acknowledgements

Robbie Joosten kindly modified the code of PDB-REDO server to enable refinement of the adduct.

References

1. Husbands, Stephen M.; Lewis, John W. **1995**. Morphinan cyclic imines and pyrrolidines containing a constrained phenyl group: high affinity opioid agonists. *Bioorganic & Medicinal Chemistry Letters,* 5(24), 2969-2974. doi.org/cbmj9g
2. Neilan, Claire L.; Husbands, Stephen M.; Breeden, Simon; Ko, Mei-Chuan; Aceto, Mario D.; Lewis, John W., . . . Traynor, John R. **2004**. Characterization of the complex morphinan derivative BU72 as a high efficacy, long-lasting μ-opioid receptor agonist. *European Journal of Pharmacology,* 499(1), 107-116. doi.org/fpdvz9
3. Huang, Weijiao; Manglik, Aashish; Venkatakrishnan, A. J.; Laeremans, Toon; Feinberg, Evan N.; Sanborn, Adrian L., . . . Kobilka, Brian K. **2015**. Structural insights into μ-opioid receptor activation. *Nature,* 524(7565), 315–321. doi.org/f7m78z

4. Smith, Richard D.; Engdahl, Alaina L.; Dunbar, James B.; Carlson, Heather A. **2012**. Biophysical limits of protein-ligand binding. *Journal of Chemical Information and Modeling,* 52(8), 2098-2106. doi.org/f36nns
5. Munro, Thomas A. **2020**. Revised (β-phenyl) stereochemistry of ultrapotent μ opioid BU72. *bioRxiv*. doi.org/dq7s
6. Huang, Weijiao; Manglik, Aashish; Venkatakrishnan, A. J.; Laeremans, Toon; Feinberg, Evan N.; Sanborn, Adrian L., . . . Kobilka, Brian K. **2020**. Author correction: Structural insights into μ-opioid receptor activation. *Nature,* 584(7820), E16. doi.org/d5jj
7. Husbands, Stephen M.; Neilan, Claire L.; Broadbear, Jillian; Grundt, Peter; Breeden, Simon; Aceto, Mario D., . . . Traynor, John R. **2005**. BU74, a complex oripavine derivative with potent kappa opioid receptor agonism and delayed opioid antagonism. *European Journal of Pharmacology,* 509(2), 117-125. doi.org/drkbg6
8. Chan, H. C. Stephen; Xu, Yueming; Tan, Liang; Vogel, Horst; Cheng, Jianjun; Wu, Dong; Yuan, Shuguang. **2020**. Enhancing the signaling of GPCRs via orthosteric ions. *ACS Central Science,* 6(2), 274-282. doi.org/dk25
9. Zou, Rongfeng; Wang, Xueying; Li, Shu; Chan, H. C. Stephen; Vogel, Horst; Yuan, Shuguang. **2021**. The role of metal ions in G protein-coupled receptor signalling and drug discovery. *WIREs Computational Molecular Science,* 12(2), e1565. doi.org/gmcwd9
10. Kuppuraj, Gopi; Dudev, Minko; Lim, Carmay. **2009**. Factors governing metal–ligand distances and coordination geometries of metal complexes. *Journal of Physical Chemistry B,* 113(9), 2952-2960. doi.org/dqgnpj
11. Kumar, K. S. Dinesh; Gurusaran, M.; Satheesh, S. N.; Radha, P.; Pavithra, S.; Thulaa Tharshan, K. P. S., . . . Sekar, K. **2015**. Online_DPI: a web server to calculate the diffraction precision index for a protein structure. *Journal of Applied Crystallography,* 48(3), 939-942. doi.org/f7fbq6
12. Isberg, Vignir; de Graaf, Chris; Bortolato, Andrea; Cherezov, Vadim; Katritch, Vsevolod; Marshall, Fiona H., . . . Gloriam, David E. **2015**. Generic GPCR residue numbers – aligning topology maps while minding the gaps. *Trends in Pharmacological Sciences,* 36(1), 22-31. doi.org/f62gpv
13. Zheng, Heping; Chordia, Mahendra D.; Cooper, David R.; Chruszcz, Maksymilian; Muller, Peter; Sheldrick, George M.; Minor, Wladek. **2014**. Validation of metal-binding sites in macromolecular structures with the CheckMyMetal web server. *Nature Protocols,* 9(1), 156-170. doi.org/dpcs
14. Masmaliyeva, Rafiga C.; Babai, Kave H.; Murshudov, Garib N. **2020**. Local and global analysis of macromolecular atomic displacement parameters. *Acta Crystallographica Section D: Biological Crystallography,* 76(10), 926-937. doi.org/jght
15. Zheng, Heping; Cooper, David R.; Porebski, Przemyslaw J.; Shabalin, Ivan G.; Handing, Katarzyna B.; Minor, Wladek. **2017**. CheckMyMetal: a macromolecular metal-binding validation tool. *Acta Crystallographica Section D: Biological Crystallography,* 73(3), 223-233. doi.org/f9tvdh
16. Dudev, Minko; Wang, Jonathan; Dudev, Todor; Lim, Carmay. **2006**. Factors governing the metal coordination number in metal complexes from Cambridge Structural Database analyses. *Journal of Physical Chemistry B,* 110(4), 1889-1895. doi.org/dbw84h
17. Kruse, Holger; Sponer, Jiri; Auffinger, Pascal. **2019**. Comment on “Evaluating unexpectedly short non-covalent distances in X-ray crystal structures of proteins with electronic structure analysis”. *Journal of Chemical Information and Modeling,* 59(9), 3605-3608. doi.org/d8jz

18. Leonarski, Filip; D'Ascenzo, Luigi; Auffinger, Pascal. **2016**. Mg^{2+} ions: do they bind to nucleobase nitrogens? *Nucleic Acids Research,* 45(2), 987-1004. doi.org/f9sg7d
19. Aurich, Hans G. **1989**. Nitroxides. In Patai, Saul & Rappoport, Zvi (Eds.), *Nitrones, Nitronates and Nitroxides* (pp. 313-370). doi.org/cp3635
20. Ihara, Hideshi; Kakihana, Yuki; Yamakage, Akane; Kai, Kenji; Shibata, Takahiro; Nishida, Motohiro, . . . Uchida, Koji. **2019**. 2-Oxo-histidine–containing dipeptides are functional oxidation products. *Journal of Biological Chemistry,* 294(4), 1279-1289. doi.org/d7n6
21. Masson, Jean-Francois; Gauda, Estelle; Mizaikoff, Boris; Kranz, Christine. **2008**. The interference of HEPES buffer during amperometric detection of ATP in clinical applications. *Analytical and Bioanalytical Chemistry,* 390(8), 2067-2071. doi.org/fhkf72
22. Simpson, Jeremy A.; Cheeseman, Kevin H.; Smith, Susan E.; Dean, Roger T. **1988**. Free-radical generation by copper ions and hydrogen peroxide. Stimulation by Hepes buffer. *Biochemical Journal,* 254(2), 519-523. doi.org/jf6h
23. Ueda, Jun-ichi; Ozawa, Toshihiko; Miyazaki, Makiko; Fujiwara, Yumiko. **1993**. SOD-like activity of complexes of nickel(II) ion with some biologically important peptides and their novel reactions with hydrogen peroxide. *Inorganica Chimica Acta,* 214(1), 29-32. doi.org/d8dbw9
24. Chaudhuri, Barnali N.; Lange, Stephanie C.; Myers, Rebecca S.; Chittur, Sridar V.; Davisson, V. Jo; Smith, Janet L. **2001**. Crystal structure of imidazole glycerol phosphate synthase: a tunnel through a $(\beta/\alpha)_8$ barrel joins two active sites. *Structure,* 9(10), 987-997. doi.org/cjmk4z
25. Chan, Peter W. Y.; Chakrabarti, Nilmadhab; Ing, Chris; Halgas, Ondrej; To, Terence K. W.; Wälti, Marielle, . . . Pai, Emil F. **2022**. Defluorination capability of L-2-haloacid dehalogenases in the HAD-like hydrolase superfamily correlates with active site compactness. *ChemBioChem,* 23(1), e202100414. doi.org/jdgn
26. Yaniv, Oren; Halfon, Yehuda; Shimon, Linda J. W.; Bayer, Edward A.; Lamed, Raphael; Frolow, Felix. **2012**. Structure of CBM3b of the major cellulosomal scaffoldin subunit ScaA from *Acetivibrio cellulolyticus*. *Acta Crystallographica Section F: Structural Biology Communications,* 68(1), 8-13. doi.org/fx9pds
27. Golovin, Adel; Henrick, Kim. **2008**. MSDmotif: exploring protein sites and motifs. *BMC Bioinformatics,* 9(1), 312. doi.org/cs84rz
28. Kirsch, Michael; Lomonosova, Elena E.; Korth, Hans-Gert; Sustmann, Reiner; de Groot, Herbert. **1998**. Hydrogen peroxide formation by reaction of peroxynitrite with HEPES and related tertiary amines: implications for a general mechanism. *Journal of Biological Chemistry,* 273(21), 12716-12724. doi.org/dhdr4m
29. Chen, Jia-Hao; Ahmed, Wasim; Li, Ming-Hua; Li, Zhao-Dong; Cui, Zi-Ning; Tang, Ri-Yuan. **2020**. TEMPO-mediated synthesis of *N*-(fluoroalkyl)imidazolones via reaction of imidazoles with iodofluoroacetate. *Advanced Synthesis & Catalysis,* 362(1), 269-276. doi.org/d7v3
30. Laulumaa, Saara; Kursula, Petri. **2019**. Sub-atomic resolution crystal structures reveal conserved geometric outliers at functional sites. *Molecules,* 24(17), 3044. doi.org/fn8x
31. Zhou, Qingtong; Yang, Dehua; Wu, Meng; Guo, Yu; Guo, Wanjing; Zhong, Li, . . . Zhao, Suwen. **2019**. Common activation mechanism of class A GPCRs. *eLife,* 8, e50279. doi.org/fpcw
32. Koehl, Antoine; Hu, Hongli; Maeda, Shoji; Zhang, Yan; Qu, Qianhui; Paggi, Joseph M., . . . Kobilka, Brian K. **2018**. Structure of the μ-opioid receptor–G_i protein complex. *Nature,* 558(7711), 547–552. doi.org/cqzg

33. Gmeiner, Peter; Wang, Haoqing; Hetzer, Florian; Huang, Weijiao; Qu, Qianhui; Meyerowitz, Justin, . . . Kobilka, Brian K. **2022**. Structure-based evolution of G protein-biased μ-opioid receptor agonists. *Angewandte Chemie International Edition,* 61(26), e202200269. doi.org/hp35
34. Wang, Haoqing; Qu, Qianhui; Skiniotis, Georgios; Kobilka, Brian K. **2022**. C5guano-*μ*OR-Gi-scFv16. *Protein Data Bank*. doi.org/h7qn
35. Robertson, Michael J.; He, Feng; Meyerowitz, Justin G.; Seven, Alpay B.; Panova, Ouliana; Peroto, Maria-Claudia, . . . Skiniotis, Georgios. **2021**. Structure determination of inactive-state GPCRs with a universal nanobody. *bioRxiv*. doi.org/g5k5
36. Che, Tao; Majumdar, Susruta; Zaidi, Saheem A.; Ondachi, Pauline; McCorvy, John D.; Wang, Sheng, . . . Roth, Bryan L. **2018**. Structure of the nanobody-stabilized active state of the kappa opioid receptor. *Cell,* 172(1), 55-67. doi.org/chz8
37. Waugh, David S. **2011**. An overview of enzymatic reagents for the removal of affinity tags. *Protein Expression and Purification,* 80(2), 283-293. doi.org/dn7skj
38. Pentony, Melissa M.; Jones, David T. **2010**. Modularity of intrinsic disorder in the human proteome. *Proteins,* 78(1), 212-221. doi.org/b5jhhp
39. Lobanov, Michail Yu; Furletova, Eugeniya I.; Bogatyreva, Natalya S.; Roytberg, Michail A.; Galzitskaya, Oxana V. **2010**. Library of disordered patterns in 3D protein structures. *PLOS Computational Biology,* 6(10), e1000958. doi.org/fmk4dn
40. Hawkins, Clare L.; Davies, Michael J. **2019**. Detection, identification, and quantification of oxidative protein modifications. *Journal of Biological Chemistry,* 294(51), 19683-19708. doi.org/gpz2xk
41. Grady, John K.; Chasteen, N. Dennis; Harris, Daniel C. **1988**. Radicals from "Good's" buffers. *Analytical Biochemistry,* 173(1), 111-115. doi.org/dv6hcg
42. Emsley, Paul. **2017**. Tools for ligand validation in Coot. *Acta Crystallographica Section D: Biological Crystallography,* 73(3), 203-210. doi.org/f9txh4
43. Nicholls, Robert. **2017**. Ligand fitting with CCP4. *Acta Crystallographica Section D: Biological Crystallography,* 73(2), 158-170. doi.org/f9ps4d
44. Joosten, Robbie P.; Long, Fei; Murshudov, Garib N.; Perrakis, Anastassis. **2014**. The PDB_REDO server for macromolecular structure model optimization. *IUCrJ,* 1(4), 213-220. doi.org/dmft
45. Smart, Oliver S.; Womack, T. O.; Sharff, A.; Flensburg, C.; Keller, P.; Paciorek, W., . . . Bricogne, G. (2011). GRADE version 1.2.19. Cambridge, United Kingdom: Global Phasing Ltd. Retrieved from grade.globalphasing.org
46. DeLano, Warren L.; Schrodinger. **2021**. PyMOL molecular graphics system, version 2.5.0. pymol.org